LAWRENCE
LIVERMORE
NATIONAL
LABORATORY

UCRL-JRNL-204389

Testing LMC Microlensing Scenarios: The Discrimination Power of the SuperMACHO Microlensing Survey

A. Rest, C. Stubbs, A. C. Becker, G. A. Miknaitis, A. Miceli, R. Covarrubias, S. L. Hawley, C. Smith, N. B. Suntzeff, K. Olsen, J.L. Prieto, R. Hiriart, D. L. Welch, K.H. Cook, S. Nikolaev, G. Proctor, A. Clocchiatti, D. Minniti, A. Garg, P. Challis, S. C. Keller, B. P. Scmidt

May 28, 2004

Astrophysical Journal

Disclaimer

Testing LMC Microlensing Scenarios: The Discrimination Power of the SuperMACHO Microlensing Survey

A. Rest[1,2], C. Stubbs[3], A. C. Becker, G. A. Miknaitis, A. Miceli, R. Covarrubias, and S. L. Hawley

Department of Astronomy, University of Washington, Box 351580, Seattle, WA 98195

C. Smith, Nicholas B. Suntzeff, K. Olsen, J. L. Prieto, and R. Hiriart

Cerro Tololo Inter-American Observatory (CTIO), La Serena, Chile

D. L. Welch

Department of Physics and Astronomy, McMaster University, Hamilton, Ontario, L8S 4M1, Canada

K. H. Cook, S. Nikolaev, and G. Proctor[4]

Lawrence Livermore National Laboratory, 7000 East Ave., Livermore, CA 94550

A. Clocchiatti[5] and D. Minniti[6]

Department of Astronomy, Pontificia Universidad Católica de Chile, Casilla 306, Santiago 22, Chile

A. Garg, and P. Challis[7]

Physics Department, Harvard University, 17 Oxford Street, Cambridge, MA 02138

and

S. C. Keller and B. P. Schmidt

Research School of Astronomy and Astrophysics, Australian National University, Weston, ACT 2611, Australia

ABSTRACT

Characterizing the nature and spatial distribution of the lensing objects that produce the observed microlensing optical depth toward the Large Magellanic Cloud (LMC) remains an open problem. We present an appraisal of the ability of the SuperMACHO Project, a next-generation microlensing survey pointed toward the LMC, to discriminate between various proposed lensing populations. We consider two scenarios: lensing by a uniform foreground screen of objects and self-lensing of LMC stars. The optical depth for "screen-lensing" is essentially constant across the face of the LMC; whereas, the optical depth for self-lensing shows a strong spatial dependence. We have carried out extensive simulations, based upon actual data obtained during the first year of the project, to assess the SuperMACHO survey's ability to discriminate between these two scenarios. In our simulations we predict the expected number of observed microlensing events for each of our fields by adding artificial stars to the images and estimating the spatial and temporal efficiency of detecting microlensing events using Monte-Carlo methods. We find that the event rate itself shows significant sensitivity to the choice of the LMC luminosity function shape and other parameters, limiting the conclusions which can be drawn from the absolute rate. By instead determining the *differential* event rate across the LMC, we can decrease the impact of these systematic uncertainties rendering the conclusions more robust. With this approach the SuperMACHO Project should be able to distinguish between the two categories of lens populations and provide important constraints on the nature of the lensing objects.

Subject headings: dark matter—microlensing—galaxies: structure—galaxies: halos—Magellanic Clouds—galaxies: individual (MWG)

---

[1]Now at Cerro Tololo Inter-American Observatory (CTIO), La Serena, Chile. CTIO is a division of the National Optical Astronomy Observatory (NOAO)

[2]Goldberg fellow

[3] Now at Departments of Astronomy and of Physics, Harvard University, Cambridge MA

[4] Now at Astronomy Dept., UC Santa Cruz, Santa Cruz, CA 95064

[5] supported from FONDECYT grant 1000524

[6] supported by Fondap Center for Astrophysics 15010003

[7]Harvard-Smithsonian Center for Astrophysics, 60 Garden St., Cambridge, MA 02138.

1. Introduction

The SuperMACHO Project is an ongoing five-year microlensing survey of the LMC that is being carried out with the specific goal (Stubbs 1999) of determining the location of the objects that produce the observed microlensing events. This paper presents an appraisal of the survey's ability to accomplish this goal. This assessment is based on extensive simulations that use actual observational data obtained during the first observing season. The LMC luminosity function plays a prominent role in this calculation, and we present an extensive analysis of this in a companion paper (Rest et al. 2004).

An elegant way to further our understanding of dark matter halos and to search for astrophysical dark matter candidates is to utilize the defining feature of the dark matter: the effect of its gravitational field. Paczynski (1986) suggested searching for dark matter (DM) in the form of MACHOs (MAssive Compact Halo Objects) using gravitational microlensing. Several groups followed this suggestion and established microlensing searches toward the LMC and other nearby galaxies. The MACHO group reported 13-17 microlensing events toward the LMC (Alcock et al. 2000b) with event timescales ranging between 34 and 230 days. This study led to an estimated microlensing optical depth toward the LMC of $\tau = 1.2^{+0.4}_{-0.3} \times 10^{-7}$. If we assume that MACHOs are responsible for this optical depth, then a typical halo model allows for a MACHO halo fraction of 20% (95% confidence interval of 8%-50%) with MACHO masses ranging between 0.15 and 0.9 $M_{\odot}$. The EROS group found 3 LMC events (Aubourg et al. 1993; Renault et al. 1997; Lasserre et al. 2000), in broad agreement with the findings of the MACHO group. The OGLE collaboration also reported one LMC microlensing event (Udalski et al. 1997). Notably, none of the surveys toward the LMC have detected events with timescales $1hr \leq \hat{t} \leq 10days$. This complete lack of short timescale events puts a strong upper limit on the abundance of low-mass DM objects: Objects with masses $10^{-7}M_{\odot} < m < 10^{-3}M_{\odot}$ make up less than 25% of the halo dark matter. Further, less than 10% of a standard spherical halo is made of MACHOs in the $3.5 \times 10^{-7}M_{\odot} < m < 4.5 \times 10^{-5}M_{\odot}$ mass range (Alcock et al. 1998).

Despite these constraints on the MACHO halo fraction, the reported microlensing event rate toward the LMC significantly exceeds that expected from known visible components of our Galaxy. This rate depends on the spatial, mass, and velocity distribution of the lenses. Unfortunately the main observable in any given microlensing event, its duration, depends upon a combination of all three of these parameters. Any conclusion about the spatial location of the lens population therefore depends upon the assumptions made about its mass and velocity. In cases where the lightcurve exhibits a departure from the "Paczynski" shape (due to a binary lens, a binary source, non-inertial motion in the lensing system, etc.), this degeneracy can be lifted, but we will defer a consideration of lightcurve fine structure

to a subsequent paper.

In light of the inherent difficulty in locating the LMC lenses down the line of sight, we are left with a variety of possible explanations for the excess LMC event rate which include: (1) lensing by a population of MACHOs in the Galactic Halo, (2) lensing by a previously undetected thick disk component of our Galaxy, (3) disk-bar or bar-bar self-lensing of the LMC, or (4) lensing by an intervening dwarf galaxy or tidal tail. Due to the limited number of events observed to date it is not yet clear which scenario or combination of scenarios explains the observed lensing. In the following, we will discuss these different populations, each of which is problematic in some respect.

1.1. Milky Way Halo Lenses?

If the lenses reside as MACHOs in the Galactic halo, the inferred mass is $0.1 - 1\,M_{\odot}$ (Alcock et al. 2000b). If we assume the lens population is comprised of some known astronomical object, the most likely candidates are white dwarfs. There are some indications that there might be a previously undetected population of old white dwarfs (WDs) in the Galaxy (Ibata et al. 1999, 2000; Méndez & Minniti 2000; Oppenheimer et al. 2001; Nelson et al. 2002), favoring this interpretation. Still, like any scenario populating the Galactic halo with stellar remnants, the halo WD explanation poses a challenge to stellar formation and evolution theory: the stellar progenitors are expected to enrich the gas and/or stars to a greater degree than has been observed. In addition, if other galaxies have similar halos, then their progenitor populations might be observable in galaxies at high redshift. There are ways out of these constraints, e.g. by assuming non-standard initial mass functions (Chabrier et al. 1996; Chabrier 1999), or by anticipating lower metal yields from old, low-metallicity main sequence progenitors, or perhaps by allowing that the processed ejecta remain in the form of hot gas as yet undetected (Fields et al. 2000). All these attempts require fine tuning of the models or invoke unlikely physics rendering them somewhat unsatisfying. The interpretation that the detected faint WDs are members of the Galactic halo is certainly not uncontested (e.g., see Richer (2001))

1.2. Thick Disk Lenses?

An alternative interpretation is that the lenses belong kinematically to the thick disk (Reid et al. 2001). In this scenario, the inferred number of WDs exceeds the number expected from the known thick disk or spheroid, forcing the invocation of an undetected very thick

disk as an alternative to a halo population of lenses (Gates et al. 1998). Gyuk & Gates (1999) showed that such disks may be able to reproduce the observed optical depth toward the LMC. More recently, they showed that the predicted properties of such a population are consistent with the observed properties of the WDs (Gates & Gyuk 2001). Since the total mass of such thick disk WDs needed to account for the observed optical depth seen toward the LMC is much smaller than the total mass needed in the halo, this explanation solves some of the stellar evolution and chemical enrichment problems. Only more detailed observations can determine to which populations the WDs might belong, or if they reside in a new, unknown component of the Galaxy.

1.3. LMC Self-lensing?

A third possible interpretation of the optical depth toward the LMC is that the lenses are not part of our Galaxy but rather of the LMC itself (denoted as LMC self-lensing). This was first suggested by Sahu (1994), and many more variations of self-lensing have since been proposed. It has been shown that self-lensing with a coplanar LMC bar and disk is not sufficient to explain the microlensing rates (Sahu 1994; Gyuk et al. 2000). Recent observations, however, indicate that there might be kinematic (carbon star sample, Graff et al. (2000), RR Lyrae stars Minniti et al. (2003)) and photometric subcomponents of the LMC (Weinberg & Nikolaev 2001; van der Marel & Cioni 2001; van der Marel 2001). The unvirialized subcomponents can be caused by the tidal interaction between the LMC, the Galaxy, and/or the SMC. Some theoretical models that invoke such unvirialized subcomponents find that the optical depth is significantly increased and may account for half or even all of the microlensing event rate (Graff et al. 2000; Zhao & Evans 2000). The predicted events show peculiarities in their photometric, kinematic and spatial distribution, which can be used to distinguish between LMC stars and the other lens population candidates. For example, one of the two near-clump MACHO events (MACHO-LMC-1) is a few tenths of a magnitude fainter than the clump, and Zhao et al. (2000) argue that this is suggestive of having the lensed source star in a distinct population spatially separated and behind the LMC (and possibly more reddened). Using Hubble Space Telescope (HST) observations, Alcock et al. (2001a) do not find any significant evidence for such systematically redder source stars, and their results marginally favor halo lensing. In addition, recent observations do not show any significant signs of kinematic outliers in the LMC (Zhao et al. 2003), restricting any additional kinematically distinct population to less than the 1% of the LMC stars.

1.4. Galactic Halo Substructure?

There has been increasing evidence that the Galactic halo is not smooth. Beside the Magellanic Stream, another full-fledged tidal stream, the Sagittarius Dwarf galaxy, which currently is passing through the Galactic disk, has been detected (Ibata et al. 1995; Yanny et al. 2000; Ivezić et al. 2000; Vivas et al. 2001; Ibata et al. 2001). There is also tentative evidence for other tidal streams in the Galactic Halo (Newberg et al. 2002) and between the Galaxy and the LMC (Zaritsky & Lin 1997). Such an intervening dwarf galaxy or tidal tails could also cause the high microlensing event rate (Zaritsky & Lin 1997; Zhao 1998).

1.5. A First Step: Foreground lenses or LMC self-lensing?

The different candidate lensing scenarios described above can be broadly categorized into two groups:

- ***Screen-lensing*** **:** Any lensing caused by a uniform (on the angular scale of the LMC) foreground lensing population. Examples are lensing by the Galactic halo or thick disk.
- ***LMC Self-lensing*** **:** Any case where the lensing population is either the same as the source population, or spatially close to the source population. Examples are LMC disk-disk, disk-bar and bar-bar lensing, and also lensing of the LMC disk by a tidal tail within the LMC.

We consider it a sensible first step to ascertain which of these is responsible for the microlensing events seen toward the LMC.

The lensing rate for self-lensing shows a strong spatial dependence (e.g. the lensing rate for LMC bar-bar lensing is proportional to N_{bar}^2, where N is the areal density of stars), whereas the lensing rate of screen-lensing is directly proportional to the number of source stars observed. The goal of the SuperMACHO project is to determine which or what mixture of these two categories causes the observed microlensing rate. One key ingredient to achieving this is to increase the number of detected events by an order of magnitude. This ten-fold improvement in detection rate will move us out of the realm of small number statistics and allow us to determine the spatial distribution of the events on the sky (see Figure 1). The other key ingredient in our recipe for success comes from exotic microlensing events. Occasionally a microlensing event displays features that result from a breakdown in the point-source, point-lens, and/or inertial motion model used to successfully model most microlensing events (e.g., see Afonso et al. (2000), Alcock et al. (2000a), and Alcock

et al. (2001b) for binary lens events). Detecting, characterizing, and exploiting these exotic microlensing events is extremely important since they can lift the degeneracy between the mass, location and transverse velocity of the lens. These exotic features occur in roughly 10% of the events seen toward the Galactic bulge. We will defer the consideration of such exotic events to a subsequent paper and will concentrate here on assessing the SuperMACHO survey's discrimination potential using only the "classical" microlensing events.

Our approach in assessing the survey's discrimination capability is to:

1. Use actual LMC images obtained with the survey instrumentation to obtain star count information for each of our fields,
2. Add simulated microlensed flux to the frames and assess the survey's event detection efficiency for each field as a function of input event parameters,
3. Estimate, for the observed LMC optical depth, the likely event statistics across the different fields under different lensing scenarios,
4. Given the anticipated event detection rates, devise statistics that maximize the survey's ability to discriminate between screen and LMC self-lensing,
5. Assess the SuperMACHO survey's sensitivity to a specific illustrative LMC self-lensing scenario, namely the displaced LMC bar model proposed by Zhao & Evans (2000).

These steps are laid out in the sections that follow. First we describe the SuperMACHO survey strategy and the image analysis pipeline of the project. Section 3 summarizes our parameterization of the LMC stellar luminosity function, an essential ingredient needed to go from the observable quantity, the number of microlensing events detected, to the physical properties of interest, in particular the mass and spatial distributions of the lens population. We present detailed luminosity function analysis in a companion paper, Rest et al. (2004). In Section 4, we then use these results to model the number of detected microlensing events for the different candidate populations, and we predict if it will be possible for SuperMACHO to distinguish between screen- and self-lensing.

2. Observations: The Implementaion of the SuperMACHO Survey

The SuperMACHO Project[1] has been allocated 150 half-nights, distributed over 5 years, on the Cerro Tololo Interamerican Observatory (CTIO) Blanco 4m telescope through the

[1]http://www.ctio.noao.edu/supermacho

NOAO Survey Program. The survey started in 2001 and will run through 2005.

We note that we have waived any proprietary data access rights, and that the Super-MACHO survey images are accessible through the NOAO Science Archive on the NOAO web site[2].

Observations are carried out every other night in dark time during the months of October, November, and December, when the LMC is most accessible from CTIO. We use the $8K \times 8K$ MOSAIC II CCD imager with a FOV of 0.33 square degree. The 8 SITe $2K \times 4K$ CCDs are read out in dual-amplifier mode (i.e. different halves of each CCD are read out in parallel through separate amplifiers) to increase our observing efficiency. In order to maximize the throughput we use a custom-made broadband filter (VR filter) from 500nm to 750nm. The atmospheric dispersion corrector on the Mosaic imager allows for the use of this broad band without a commensurate PSF degradation.

In devising an observing strategy we want to find a good balance between maximizing the number of events detected and assuring a uniform spatial coverage. The work described here has guided our decisions on how to best spend the telescope time on the sky. We have defined a grid of 68 fields over the face of the LMC. Previous microlensing surveys found that the distribution of microlensing event durations toward the LMC has its peak at about 80 days, with virtually no event lasting less than two weeks. In order to sample the lightcurves adequately and sufficiently, we observe all fields every other night during dark time. This also serves to equalize, to first order, the event detection efficiency due to sampling effects across the fields. There remains the field-dependent detection efficiency due to the different stellar densities and due to intentional inequality in exposure times.

The distribution of the available observing time in a half-night across the LMC is driven by two conflicting considerations: the need to maximize the number of stars that we monitor and the need to survey as large a region as possible in order to discriminate between the different candidate lens populations. If the only goal were to maximize the number of monitored stars, and conseqently the number of detected microlensing events, we would concentrate on deep exposures of the central region of the LMC. Maximizing the number of microlensing events is, however, less important than achieving maximum discrimination between models.

We have adopted the strategy outlined by Gould (1999) to achieve a distribution of exposure times that maximizes the microlensing event rate subject to the constraints of a given spatial sampling and the differing sensitivity between the inner and outer regions of

[2]ftp://archive.tuc.noao.edu/pub/

the LMC. The basic idea is that the distribution of exposure times for a microlensing survey is optimized when a shift of δt in exposure from field A to field B gains as many stars in B as are lost in field A. At this extremum $\frac{\delta N_A}{\delta t} = \frac{\delta N_B}{\delta t}$. This condition must be achieved subject to two constraints. First, the total exposure time plus the total time spent on readout must equal the number of workable hours in a half night. The second constraint is that the number of sources monitored in the inner and outer regions of the LMC must be balanced to achieve the desired spatial coverage.

We have used the stellar density normalizations described in section 3 and a simple division of inner and outer fields to optimize the distribution of exposure times given the properties of the MOSAIC imager on the CTIO 4m telescope. We have set a minimum exposure time of 25 seconds, in order to assure coverage of the sparser fields, and a maximum exposure time of 200 seconds in order to avoid saturation effects.

The SuperMACHO Project started observations in Sept 2001. The data analysis pipeline is currently implemented as a combination of C code, IRAF, Perl and Python scripting tied together to provide an integrated but modular environment (Smith et al. 2002).

The first steps of the data processing, crosstalk correction and astrometric calibration, are best done on the whole image because the units are not completely independent. The rest of the image reduction, as well as all of the transient analysis, breaks down naturally into 16 independent units, the amplifier-images[3], and can therefore be efficiently handled in parallel. We employ a cluster of 18 CPUs with a 6.5 Terabyte redundant disk array.

Standard photometry of transient or variable objects becomes inefficient in highly crowded images; therefore, we use a method called difference image analysis (DIA) which has rapidly evolved in the last few years. The first implementation was done by Phillips & Davis (1995) who introduced a method that registered images, matched the point spread function (PSF), and matched the flux of objects in order to detect transients. Derivatives of DIA have been widely applied in various projects (e.g., MACHO, Alcock et al. (1999); M31 microlensing, Crotts et al. (1999); OGLE, Wozniak (2000); WeCAPP, Gössl & Riffeser (2002); DLS, Becker (2002)). Since the PSF varies over the field of view due to optical distortions or out-of-focus images, for example, it is essential to use a spatially varying kernel (Alard & Lupton 1998; Alard 2000).

One of the main problems with the image differencing approach is that there are more residuals, e.g. cosmic rays and bleeds, than genuinely variable objects in the difference image. Therefore a standard profile-fitting software like DoPHOT has problems determining

[3]The Mosaic has 8 CCDs. Each CCD is read out by two amplifiers

the proper PSF used to perform photometry in the difference image. When the difference image is analyzed with our customized version of DoPHOT, we force the PSF to be the one determined for the original, flattened image. Applying this a priori knowledge of the PSF helps to guard against bright false positives, such as cosmic rays and noise peaks, which generally do not have a stellar PSF.

All detections are added into a database. Once the database is loaded and objects have been identified, queries are performed on new objects which are then classified. Objects of interest are then passed to a graphical user interface displaying stamps from image, template, and difference image for visual classification and interpretation

3. LMC luminosity functions

In order to determine the optical depth from the observable quantities (the number and duration of detected events), the number of observed stars must be known. This depends on both exposure depth and on the luminosity function (LF) of the source star population. The LMC LF is essential for the analysis (and prediction) of microlensing event rates.

We present our detailed analysis of the LMC luminosity function in a companion paper (Rest et al. 2004) and summarize its results here. Our basic approach is to compute the likely event rate distributions for a set of trial luminosity functions that span what we consider a plausible range of faint-end luminosity distributions. The star counts in each field are given an independent overall normalization, which is based upon completeness-corrected images from the first season's observations. These star counts are determined in the VR filter in which we observe.

We divided each of the 68 fields that we observe into 16 subfields based on the area covered by the Mosaic amplifiers (see Figure 1). For each of these subfields, we determined an independent LF. First, we fit a single power law to the bright end of the LF with a superimposed Gaussian function representing the red clump:

$$\Phi^*(M) \;=\; \Phi_0 10^{\beta M} + \frac{N_{RC}}{\sigma_{RC}\sqrt{2\pi}} \exp\left[-\left(\frac{M_{RC} - M}{2\sigma_{RC}} \right)^2 \right] \qquad (1)$$

where N_{RC}, M_{RC}, and σ_{RC} are the total number, the average magnitude, and the spread of red clump stars, respectively. This gives an overall normalization of the star density in a given field. The magnitude M is corrected for the exposure time t as

$$M \;=\; -2.5 \log f + 25 + 2.5 \log t \qquad (2)$$

Note that the magnitude M is *not* the calibrated absolute magnitude. Instead we choose a zero-point of 25 magnitudes as a typical offset. However, the value of this offset is not important since we use the peak magnitude of the red clump as a reference point to compare our LF to the LFs in the literature. Using such a reference point eliminates to first order the color differences between the different filter systems and also any shift of the LF due to reddening and/or absorption. Since the color of the main sequence stars changes monotonically with their birghtness, there will be small differences in LF shape between the different filter systems. For the purpose of this paper, however, these differences in shape are not bigger than the intrinsic shape differences between the LF candidates discussed and thus should not bias our results.

With our dataset it is not possible to determine the LF at the faint end correctly. High resolution HST images can help, but they lack spatial coverage due to the limited field of

view, and there are completeness corrections even with HST data. Instead of attempting to determine the exact LF for each of the subfields, we construct 5 different trial LFs. This allows us to test what systematic effect the choice of LF introduces. Figure 2 shows these different LFs. The short-dashed red line, long-dashed red line, dot-short-dashed blue line, and dot-long-dashed black line in Figure 2 are the solar neighborhood LF based on the empirical mass-luminosity function (Φ_A), the solar neighborhood LF based on the semi-empirical mass-luminosity function (Φ_B), the best guess LF (Φ_C), and the lower limit LF ($\Phi_<$), respectively. The black dotted line is the single power law ($\Phi_>$) for which the predicted (solid lines) fits best the observed object distribution at the bright end (green filled circles), and is clearly the upper bound to plausible LFs. We parametrize these LFs as a combination of three power laws:

$$\Phi(M) = \begin{cases} \Phi_1 10^{\beta_1 M} & : \quad M < M_1 \\ \Phi_1 10^{(\beta_1-\beta_2)M_1} 10^{\beta_2 M} & : \quad M_1 \leq M < M_2 \\ \Phi_1 10^{(\beta_1-\beta_2)M_1+(\beta_2-\beta_3)M_2} 10^{\beta_3 M} & : \quad M \geq M_2 \end{cases} \tag{3}$$

where M is defined in Equation 2. Some of our candidate LFs are only single or double power-laws, and in these cases we disregard the functions which do not apply. Our companion paper (Rest et al. 2004) presents the fitted parameters for the monitored LMC regions.

We will use these different trial luminosity functions in the following section where we predict event rates in different microlensing scenarios. We show that a differential analysis of the data can discriminate between models independent of the actual underlying luminosity function.

4. Event Rate Prediction

The SuperMACHO Project's initial goal is to distinguish between two broad categories of lensing: screen-lensing and self-lensing. We use data from the first year to predict the number of detected microlensing events from the different candidate populations in order to test if the SuperMACHO Project is able to distinguish between them. We add artificial stars to the images and determined the completeness of the detections. Using that, we estimate the spatial and temporal efficiency of detecting microlensing events in our data sets. In combination with the stellar luminosity functions described above, we then predict and compare the number of microlensing events for screen-lensing and self-lensing scenarios.

The number of observed events depends on both the source and lens populations. In general, calculating the expected number of events is complicated as it requires detailed knowledge about number density, velocity distribution, and other properties of the population. A good approximation is given by:

$$N_{ml} \;=\; N_{obs}\,\tau\,\mathcal{E}_t \tag{4}$$

where N_{obs} is the number of monitored stars for which microlensing can be detected, τ is the microlensing optical depth, and $\mathcal{E}_t$ is the sampling efficiency. This approximation separates the photometric and temporal completeness which makes the calculation much simpler. The number of monitored stars contains the photometric completeness and is

$$N_{obs} \;=\; \int \Phi(M)\mathcal{E}(M)\,dM \tag{5}$$

where $\mathcal{E}(M)$ is the efficiency of detecting microlensing for a star with magnitude M, and $\Phi(M)$ is the luminosity function. The temporal completeness is contained in $\mathcal{E}_t$ as

$$\mathcal{E}_t \;=\; \left(\int \left(\frac{\hat{t}}{T}\right)\,\frac{D(\hat{t})}{P_T(\hat{t})}\,d\hat{t}\right)^{-1} \tag{6}$$

where T is the effective survey duration, $\hat{t}$ is the duration of a microlensing event, $P_T(\hat{t})$ is the probability that the event is detected within T given the temporal cadence of the survey, and $D(\hat{t})$ is the normalized distribution of $\hat{t}$.

We calculate N_{obs} and $\mathcal{E}_t$ independently for each field and amplifier, as described next.

4.1. Number of Observed Stars

The best way to estimate the number of observed stars is to do Monte Carlo simulations with all the images used. The shortcoming of this method is that it is very CPU-intensive and

terabytes of images have to be simultaneously available on disk. Our goal is to predict a lower limit on the number of events; therefore, we choose a slightly different approach performing Monte Carlo simulations on only a subset of images and subject to certain assumptions.

The question we have chosen to answer is: What is the probability $\mathcal{E}(M)$ that the flux of a star with a given magnitude M is amplified during a microlensing event so that it can be detected? Let's assume that a microlensing event is potentially detectable if the difference flux at peak has a signal-to-noise ratio $S/N \geq 5$. Whether such an event is then indeed detected depends on the temporal cadence as well as the seeing and transparency of the observing nights, and we fold this into the temporal completeness analysis in Section 4.2.

The amplification of the flux during a microlensing event can be expressed as $A = (u^2+2)/(u\sqrt{u^2+4})$, where u is the angular separation between source and lens in units of the Einstein angle. Using Equation 2, we can then write the instrumental flux difference as

$$\Delta M'_{max}(M, t, u_0) \;=\; M - 25 - 2.5\log(t) - 2.5\log(A_{max} - 1) \tag{7}$$

where A_{max} and u_0 are the amplification and angular separation at maximum brightness respectively. By adding artificial stars, we estimate the completeness $C(\Delta M')$ of detections for a given instrumental flux difference with $S/N \geq 5$. Then we can estimate the probability that a microlensed star with intrinsic magnitude M has a change in flux whose $S/N \geq 5$ at maximum amplification:

$$\mathcal{E}(M) \;=\; \int C(\Delta M'_{max}(M, t, u_0))\, du_0 \tag{8}$$

With Equation 5, the number of observed stars N_{obs} can then be calculated using the luminosity function $\Phi(M)$ for a given field and amplifier (see Section 3).

4.2. Sampling efficiency

The temporal cadence and observing conditions like seeing and transparency clearly have an impact on event detection efficiency. This is folded into $P(\hat{t})$ and thus implicitly into $\mathcal{E}_t$ (see Equation 6).

In order to estimate $P(\hat{t})$ we perform Monte-Carlo simulations. During each year microlensing events are drawn at random to have peak amplification sometime during an interval of $T = 300$ days. This interval is dictated by the extent of the period of actual data-taking (100 days) and the need to ensure that real events which reach peak amplification before or after that interval (but are observable during the data-taking) are represented in the simulation. The 100-day padding at both ends of the observation period is driven

by the typical $\hat{t}$ found by the MACHO Project. The SuperMACHO observation periods are usually allocated in three runs of about ten nights of bi-nightly observing separated by two weeks. Factors such as weather, instrument failures, and computer down time are taken into account by randomly eliminating one out of four nights. For a given $\hat{t}$, we realize 1000 lightcurves for each microlensing impact parameter $u_0 = 0.0125, 0.0375, ..., 0.4875$. The time of maximum is randomly chosen within T. As a lower limit, we assume that all microlensing events observed have a difference flux with $S/N\,(W_0, t_0) = 5$, where W_0 is the $FWHM$ of the seeing at time t_0 of maximum amplification. Then the S/N of a detection on another night can be estimated as

$$S/N\,(W,t) = \left(\frac{W_0}{W}\right)^2 \frac{A(t)-1}{A_{max}-1} S/N\,(W_0,t_0) \tag{9}$$

$$\tag{10}$$

We randomly draw W_0 and W from the distribution of seeing in the first year of operation (see Figure 3). We want to emphasize that this is conservatively a lower limit, since the stars we count in N_{obs} have a $S/N \geq 5$ in the difference flux at maximum amplification; whereas, our Monte-Carlo simulations assume $S/N = 5$ at peak.

So for each lightcurve we have estimated the S/N for every night with useful data based on the $FWHM$ and amplification. The decision whether we do or do not detect such a lightcurve is based on the following additional criteria:

- At least 2 detections on the rising arm of the lightcurve with a $S/N > 2.0$
- At least 4 detections have a $S/N > 2.0$

This ensures that the events are "contained" within the survey coverage time and that there are enough significant detections to "trigger" an alert for follow-up observations. The upper panel of Figure 4 shows the probability $P\left(\hat{t}\right)$ to detect a microlensing event with event duration of $\hat{t}$. Clearly, it is easier to detect a microlensing event with long duration. Note that the probability is well below 1.0. This is because we use $T = 300$ days, much longer than the real time interval our observations span (~ 100 days), and the probability of detecting an event with a t_0 well outside the time the observations are taken is rather small. However, this effectively cancels out later on since we multiply by T when calculating $\mathcal{E}_t$ (see Equation 6).

A more intuitive measure is $P\left(\hat{t}\right) \times T/\hat{t}$, which is the number of microlensing events detected per $1/\tau$ stars during T assuming that all microlensing events have an event duration of $\hat{t}$ (see lower panel of Figure 4). The decrease of detection probability for decreasing event duration is countered by that fact that for smaller event durations more microlensing events happen per $1/\tau$ stars in the given observing time. This causes the peak at $\hat{t} \sim 50$ days.

Existing microlensing event statistics suggest that the event rate distribution has a strong peak at about 80 days (Alcock et al. 2000b). Therefore we choose as $D(\hat{t})$ a Gaussian distribution with the peak at 80 days and with a spread of 20 days. Using Equation 6, we can now evaluate

$$\mathcal{E}_t \sim 0.8 \tag{11}$$

Thus we will observe about 0.8 microlensing events per $1/\tau$ observed stars in 1 year.

4.3. Bar-Disk Self-lensing Models for the LMC

The optical depth of self-lensing is still a matter of controversy. Some studies find rather small values in the range of $1.0 - 8.0 \times 10^{-8}$ (e.g. Alcock et al. (1997), Gyuk et al. (2000), and Jetzer et al. (2002)); whereas, other studies suggest optical depths up to 1.5×10^{-7} (e.g. Zhao & Evans (2000)). This controversy arises from the still rather imprecise knowledge of the structure of the LMC and consequent differences in the adopted models.

The Zhao & Evans (2000) models derived in their paper are concrete and testable self-lensing models which we will use in the following sections to predict the SuperMACHO self-lensing event rate. As pointed out above, these models (denoted as model set *A*, see following Section) predict a rather large optical depth and are thus more favorable to a self-lensing interpretation of LMC microlensing. We then improve upon their models (see Section 4.3.2) for an alternative, more realistic model set, denoted as model set *B*. This allows us to make a direct spatial comparison between self-lensing and screen-lensing event rates.

4.3.1. Zhao & Evans (2000) Model Set A

Zhao & Evans (2000) derive in their paper concrete and testable self-lensing models. In this section we describe this derivation, which we will use in the next section to predict the SuperMACHO self-lensing event rate.

We define a coordinate system with X, Y, and Z being decreasing right ascension, increasing declination, and line-of-sight direction centered at the optical center of the LMC bar, where X, Y, and Z are in units[4] of kpc. The star count density of the disk (I_d) can

[4]For the LMC, 1 kpc is roughly 1 degree

then be parametrized as an exponential disk, whereas the bar (I_b) is best characterized with boxy contours and sharp edges:

$$I_d(X_d, Y_d) = \frac{N_0(1-f_b)}{2\pi L_d W_d} \exp\left(-\sqrt{\frac{X_d^2}{L_d^2} + \frac{Y_d^2}{W_d^2}}\right) \quad (12)$$

$$I_b(X_b, Y_b) = \frac{N_0 f_b}{3.286 L_b W_b} \exp\left(-\frac{X_d^4}{L_d^4} - \frac{Y_d^4}{W_d^4}\right) \quad (13)$$

where N_0 is a normalization factor[5], and f_b is the fraction of the LMC stars in the bar. Here (X_b, Y_b) is the coordinate system rotated by the position angle θ_b such that the axes coincide with the apparent major and minor axes of the bar, and (L_b, W_b) are the characteristic length and width of the bar. Similarly, (X_d, Y_d) is the rotated and displaced natural coordinate system of the bar, and (L_d, W_d) its characteristic length and width, respectively.

$$X_b = X \sin\theta_b - Y \cos\theta_b \quad (14)$$

$$Y_b = X \cos\theta_b + Y \sin\theta_b \quad (15)$$

$$X_d = (X - 0.46) \sin\theta_d - (Y - 0.70) \cos\theta_d \quad (16)$$

$$Y_d = (X - 0.46) \cos\theta_d + (Y - 0.70) \sin\theta_d \quad (17)$$

The vector $(0.46, 0.70)$ is the apparent displacement between the bar and disk in the (X, Y) plane. In the following we use the default model parameters given in Table 3, which are motivated by observations in optical bands and in the Deep Near-Infrared Survey (DENIS) J, H, and K bands (e.g., Cioni et al. (2000)). Assuming that on average the stars in the disk and bar have the same mass, i.e. a constant conversion factor M_{LMC}/N_0, one can calculate the surface density of all stars in the LMC as

$$\Sigma(X, Y) = \frac{(I_b + I_d) M_{LMC}}{N_0} \quad (18)$$

Note that N_0 cancels out if I_b and I_d are inserted (see Equation 12 and 13). The line-of-sight separation Δ_{bd} between the midplanes of the two structures (bar and disk) can be approximated as

$$\Delta_{bd}(X, Y) = |Z_0 + c_1 X + c_2 Y| \quad (19)$$

The dimensionless constants c_1 and c_2 depend on the inclinations of the planes, and can be estimated as $c_1 \sim \tan i_b - \tan i_d \sim 0.7$ and $c_2 \sim 0$. The latter is true since the distance moduli show predominantly an east-west gradient. The elevation Z_0 indicates the level of

[5]This normalization factor drops out in Equation 18

displacement between the disk and the bar. The average separation between source and lens is then given as

$$\Delta(X,Y) \;=\; \frac{I_b^2\Delta_b + I_d^2\Delta_d + I_b I_d \max(\Delta_b+\Delta_d, \Delta_{bd})}{(I_b+I_d)^2} \tag{20}$$

where the terms in the numerator characterize the self-lensing of the bar, the disk, and between the bar and disk, respectively. The line-of-sight depth of the bar and disk are denoted as Δ_b and Δ_d, respectively. In the limit in which the source and the lens are at roughly the same distance, the optical depth can then be expressed as

$$\tau(X,Y) \;\sim\; 10^{-7}\frac{\Sigma(X,Y)}{160\ M_\odot\ \mathrm{pc}^{-2}}\frac{\Delta(X,Y)}{1\ \mathrm{kpc}} \tag{21}$$

The value of τ depends mainly on two parameters: the displacement Z_0 between the disk and the bar and the mass of the bar defined by the mass fraction f_b. In the following, we will vary these parameters to estimate the spatially varying optical depth for different model realizations, and we denote this set of models as model set A.

4.3.2. Zhao & Evans (2000) Model Set B

The optical depth range for self-lensing found by Zhao & Evans (2000) is significantly larger than the ones found by other studies (e.g. Alcock et al. (1997), Gyuk et al. (2000), and Jetzer et al. (2002)). As an alternative to model set A, we modify the original Zhao & Evans (2000) models by improving the effective separation $\Delta'(X,Y)$ (Nikolaev, private communication) which significantly decreases the optical depth:

$$\Delta'(X,Y) \;=\; \frac{I_b^2\Delta_b/6 + I_d^2\Delta_d/6 + I_b I_d \Psi(\Delta_b+\Delta_d, \Delta_{bd})}{(I_b+I_d)^2} \tag{22}$$

where the function Ψ is

$$\Psi(\Delta_b+\Delta_d,\Delta_{bd}) \;=\; \begin{cases} \Delta_{bd} & : \quad \Delta_{bd} > (\Delta_b+\Delta_d)/2 \\ \Delta_{bd} + ((\Delta_b+\Delta_d)/2 - \Delta_{bd})^3/(3\Delta_b\Delta_d) & : \quad \Delta_{bd} \le (\Delta_b+\Delta_d)/2 \end{cases} \tag{23}$$

Note that the first two terms of $\Delta'(X,Y)$, the contributions of disk-disk and bar-bar self-lensing, are smaller by a factor of six compared to the equivalent expression in the Zhao & Evans (2000) calculations (see Equation 20). This takes geometrical considerations into account since source and lens population are the same. The third term is a better approximation for the disk-bar separation: The two cases in Equation 23 represent situations when 1) disk and bar are well separated along the line of sight and 2) when they overlap each other. The two limiting cases produce the same result when $\Delta_{bd} = (\Delta_b+\Delta_d)/2$.

It is also important to note that the Zhao models have unrealistically high projected central surface densities, reaching $640\,\mathrm{M}_\odot\,\mathrm{pc}^{-2}$. A model with parameters as in Gyuk et al. (2000) leads to central densities on the order of $300\,\mathrm{M}_\odot\,\mathrm{pc}^{-2}$. The discrepancy is due to the very heavy bar ($f_b = 0.5$) and the quartic bar model (which is more centrally concentrated than a Gaussian bar) used by Zhao & Evans (2000). Clearly, less centralized projected surface densities result in a decrease of the central self-lensing optical depth.

We repeat the same simulation as we have done with the Zhao & Evans (2000) models but substituting $\Delta(X, Y)$ with $\Delta'(X, Y)$. These models are denoted as self-lensing model set *B*.

4.4. Discriminating between Halo-lensing and LMC self-lensing

In this section, we combine the results from the previous sections in order to obtain a quantitative prediction of the number of observed microlensing events. The main difference between self-lensing and screen-lensing is that the lensing rates show a different spatial dependence; therefore, we calculate separately for each field and amplifier the expected number of observed microlensing events using Equation 4.

First, we estimate the number of observed stars N_{obs} for each field and amplifier using Equation 5 as described in Section 4.1. Figure 5 illustrates this for the example field sme9. The upper panel shows the luminosity functions, the middle panel shows the efficiency[6], and the lower panel shows the number of useful observed stars per magnitude, which is the product of the two upper panels. The two competing effects, increasing LF and decreasing efficiency for increasing magnitude, cause a peak at $M \sim 22.5$, and the magnitude range $21 < M < 24$ will contribute most to the observed microlensing event rate. The upper panel of Figure 6 shows the total number of observed stars per magnitude bins for all fields and amplifiers added up. We obtain the total number of observed stars by integrating over magnitude (see lower panel). Not surprisingly, the LF chosen does significantly impact the estimated number of observed stars, e.g., choosing Φ_B (short-dashed red line) results into ~ 2 times more observed stars than Φ_C (dot-short-dashed blue line). The temporal completeness is taken into account by using $\mathcal{E}_t \sim 0.8$ (see Section 4.2).

We can now calculate N_{ml} for any field, amplifier, and optical depth τ. As optical depth for screen-lensing we use 1.2×10^{-7} as determined by the MACHO Project (see Alcock

[6]The efficiency levels out at about 50% since we integrate in Equation 8 from 0 to only 0.5, and not to 1, due to the fact that we do not consider events with amplification smaller than 2

et al. 2000b). For self-lensing, we use the Zhao & Evans self-lensing model sets A and B (see Section 4.3). The spatially varying τ for each of these models is calculated using each possible combination of $f_b = [0.3, 0.4, 0.5]$, and $Z_0 = [-1, -0.5, 0, 0.5, 1]$, where f_b is the mass fraction of the bar, and Z_0 is the level of displacement between the disk and the bar in kpc. Based on observations, this covers the likely parameter space of f_b and Z_0. The fields are divided into sets 1-5, based on their respective star density determined with the Zhao & Evans (2000) LMC bar model (see Figure 1). Set 1 is the most crowded (yellow) and set 5 is the least crowded set (green). For each set of fields, we add up the predicted number of microlensing events for the different models and LFs. The upper panel of Figure 7 shows for each set of fields the number of microlensing events for Zhao LMC self-lensing model set A (open black circles), model set B (open blue squares), and screen-lensing (closed red circles). For clarity the open symbols are plotted with a slight offset for a given set. Note that the spread of microlensing events for screen-lensing is solely due to the different LFs (Φ_A, Φ_B, and Φ_C) used (see Figure 2). For self-lensing, an additional source of spread is caused by using different values of f_b and Z_0. Clearly, for sets 1-3 the intrinsic difference in event rate for self- and screen-lensing is of the same order as the systematic errors. The event rate for self-lensing at the center of the bar is particularly large if the displacement between the disk and the bar is large ($|Z_0| = 1$). For the two outer sets, however, the rate of self-lensing strongly decreases and is well below the event-rate for screen-lensing.

The intrinsic problem of drawing conclusions from the event rate is that there is a large spread in the predicted rate for a given field due to systematic biases, e.g. depending on what kind of LMC or Galaxy model is used, and the shape of the LF especially at the faint end. A way out of this dilemma is to go from an absolute measurement to a relative measurement: instead of considering the event rates, we investigate the differential event rate for a given field defined as the ratio of event rate of the field to the total event rate of all fields (see lower panel of Figure 7). Clearly, the spread compared to the upper panel is greatly diminished. To zeroth order all systematic errors cancel out, and the measurement is much more robust. Table 5 shows the differential event rates for self and screen-lensing. Since the number of events observed is small and is Poissonian in nature, we represent the results in confidence level plots, for which we use the approximations given in Gehrels (1986). Because the differences between self and screen-lensing are most pronounced in the outer field sets, we will investigate field set 5, and then the combined field sets 4 and 5.

Taking Poisson uncertainties into account, Figure 8 shows the 90% (dot-dashed black line), 99% (dashed black line), and 99.5% (solid black line) lower limit confidence levels for the field set 5 differential microlensing event rate. The black shaded areas are the areas excluded with a 99.5% confidence. The confidence levels are calculated by assuming that a total of 30 microlensing events are detected, which is a lower limit. The x-axis is the

observed differential event rate; whereas, the y-axis is the underlying, real differential event rate. That means for a given observed differential event rate, the black solid line indicates the maximum differential rate which can be excluded with 99.5% confidence.

How can we use this plot? As a *Gedankenexperiment*, let us assume that screen-lensing is indeed the underlying mechanism. In that case, the expectation value for the differential event rate for field set 5 is 0.152 for the least favorable LF (see Column (3) in Table 5). Clearly, the observed differential rate will be different than 0.152 due to the Poisson nature of the event rate, but most likely it will be somewhere between 0.1 and 0.2. (As a guide, the differential rate expectation value is indicated with a red dotted line.) The question is, can we exclude self-lensing? The upper limit of the differential rate of all Zhao self-lensing models in set A is 0.014 (see Column (5) in Table 5 and the blue, long-dashed line in the confidence plot). We can exclude these models with 99% and 99.5% confidence if we observe a differential rate larger than 0.11 and 0.13, respectively. Similarly for model set B, the maximum differential rate is 0.011 (blue short-dashed line), thus they can be excluded at 99.5% confidence if the observed differential event rate is bigger than 0.12. Since in our Gedankenexperiment we most likely will measure a differential rate above 0.11, we can then exclude self-lensing.

The upper limit is not as stringent. The upper panel of Figure 9 shows the upper limit confidence levels assuming that no microlensing event was detected in field set 5. The x-axis is the total number of detected microlensing events. The y-axis is the underlying, real differential rate. In that case, we can exclude screen-lensing (assuming a differential rate of 0.152, see Column (3) in Table 5 and dotted red line) only with a confidence of 90%. Considering the combined field sets 4 and 5, we can exclude self-lensing with a confidence level greater than 99.5% if we don't find any microlensing event in these field sets (see middle panel). If we assume a total of 30 events and a self-lensing differential rate of 0.055 for field sets 4 and 5, we can expect to detect one or even two events in these fields. Detecting only one event in these fields only allows us to exclude screen-lensing with 99% confidence (see lowest panel).

In reality, the microlensing is probably not caused by a single lens population, but rather by a mixture of several populations. We can expect that it will be more difficult to differentiate between the populations. Still, very recent work reinvestigating MACHO and EROS2 events finds that even though some of the events are due to self-lensing, the total event rate and spatial distribution cannot be explained by self-lensing alone (Jetzer et al. 2002). Also, a large spectroscopic survey targeting kinematic outliers in the LMC did not find evidence for a significant additional, kinematically distinct, population in the LMC (Zhao et al. 2003). The lack of such a population constrains the optical depth of self-lensing

to values too small to explain the observed event rate. Even if screen-lensing is the cause for only a fraction of the observed event rate, we will be able to detect enough events in the outer field sets to exclude self-lensing as the sole lensing mechanism toward the LMC. If self-lensing is excluded as the sole lensing mechanism, the SuperMACHO event rate will provide a lower limit on the number of MACHOs in the halo of the MW and thus provide a lower limit of their contribution to the MW's dark matter.

5. Conclusions

The reported microlensing event rate toward the LMC exceeds that expected from known visible components of our Galaxy, and the source of this observed excess rate is still the subject of discussion. Determining the nature of the lens population will have a great impact on our understanding of Galactic and LMC structure and possibly on the nature of dark matter. Possible explanations for the observed lensing can be broadly categorized into screen-lensing and self-lensing scenarios. Using the first year data of the SuperMACHO Project, we performed completeness analysis by adding artificial stars to the images and estimated the spatial and temporal efficiency of detecting microlensing events in our data sets. We predicted a lower limit of observable microlensing events for both categories using the efficiency in combination with the stellar luminosity functions. We find that the SuperMACHO Project will be able to distinguish between the two categories using the spatial differences in optical depth. Utilizing the differential event rate instead of the event rate itself decreases the impact of systematic errors rendering the results and conclusions more robust.

6. Acknowledgements

The SuperMACHO survey is being undertaken under the auspices of the NOAO Survey Program. We are very grateful for the support provided to the Survey program from the NOAO and the National Science Foundation We are particularly indebted to the scientists and staff at the Cerro Tololo Interamerican Observatory for their assistance in helping us carry out the SuperMACHO survey. We also appreciate the invaluable help of Mr. Chance Reschke in building and maintaining the computing cluster we use for image analysis.

The support of the McDonnell Foundation, through a Centennial Fellowship awarded to C. Stubbs, has been essential to the SuperMACHO survey. We are most grateful for the Foundation's support for this project.

KHC's, SN's and GP's work was performed under the auspices of the U.S. Department of Energy, National Nuclear Security Administration by the University of California, Lawrence Livermore National Laboratory under contract No. W-7405-Eng-48.

DLW acknowledges financial support in the form of a Discovery Grant from the Natural Sciences and Engineering Research Council of Canada (NSERC).

REFERENCES

Afonso, C., et al. 2000, ApJ, 532, 340

Alard, C. 2000, A&AS, 144, 363

Alard, C., & Lupton, R. H. 1998, ApJ, 503, 325

Alcock, C., et al. 1998, ApJ, 499, L9

Alcock, C., et al. 2000a, ApJ, 541, 270

Alcock, C., et al. 1999, ApJS, 124, 171

Alcock, C., et al. 1997, ApJ, 486, 697

Alcock, C., et al. 2000b, ApJ, 542, 281

Alcock, C., et al. 2001a, ApJ, 552, 582

Alcock, C., et al. 2001b, ApJ, 552, 259

Aubourg, E., et al. 1993, Nature, 365, 623

Becker, A. C. 2002, American Astronomical Society Meeting, 200, 0

Chabrier, G. 1999, ApJ, 513, L103

Chabrier, G., Segretain, L., & M'era, D. 1996, ApJ, 468, L21

Cioni, M.-R. L., Habing, H. J., & Israel, F. P. 2000, A&A, 358, L9

Crotts, A. C. S., Uglesich, R., Gyuk, G., & Tomaney, A. B. 1999, in ASP Conf. Ser., 182, Galaxy Dynamics - A Rutgers Symposium, 409

Fields, B. D., Freese, K., & Graff, D. S. 2000, ApJ, 534, 265

Gössl, C. A., & Riffeser, A. 2002, A&A, 381, 1095

Gates, E. I., & Gyuk, G. 2001, ApJ, 547, 786

Gates, E. I., Gyuk, G., Holder, G. P., & Turner, M. S. 1998, ApJ, 500, L145

Gehrels, N. 1986, ApJ, 303, 336

Gould, A. 1999, ApJ, 517, 719

Graff, D. S., Gould, A. P., Suntzeff, N. B., Schommer, R. A., & Hardy, E. 2000, ApJ, 540, 211

Gyuk, G., Dalal, N., & Griest, K. 2000, ApJ, 535, 90

Gyuk, G., & Gates, E. 1999, MNRAS, 304, 281

Ibata, R., Irwin, M., Bienaymé, O., Scholz, R., & Guibert, J. 2000, ApJ, 532, L41

Ibata, R., Lewis, G. F., Irwin, M., Totten, E., & Quinn, T. 2001, ApJ, 551, 294

Ibata, R. A., Gilmore, G., & Irwin, M. J. 1995, MNRAS, 277, 781

Ibata, R. A., Richer, H. B., Gilliland, R. L., & Scott, D. 1999, ApJ, 524, L95

Ivezić, Ž., et al. 2000, AJ, 120, 963

Jetzer, P., Mancini, L., & Scarpetta, G. 2002, A&A, 393, 129

Lasserre, T., et al. 2000, A&A, 355, L39

Méndez, R. A., & Minniti, D. 2000, ApJ, 529, 911

Minniti, D., Borissova, J., Rejkuba, M., Alves, D. R., Cook, K. H., & Freeman, K. C. 2003, Science, 301, 1508

Nelson, C. A., Cook, K. H., Axelrod, T. S., Mould, J. R., & Alcock, C. 2002, ApJ, 573, 644

Newberg, H. J., et al. 2002, ApJ, 569, 245

Oppenheimer, B. R., Hambly, N. C., Digby, A. P., Hodgkin, S. T., & Saumon, D. 2001, Science, 292, 698

Paczynski, B. 1986, ApJ, 304, 1

Phillips, A. C., & Davis, L. E. 1995, in ASP Conf. Ser., 77, Astronomical Data Analysis Software and Systems IV, Vol. 4, 297

Reid, I. N., Sahu, K. C., & Hawley, S. L. 2001, ApJ, 559, 942

Renault, C., et al. 1997, A&A, 324, L69

Rest, A., et al. 2004, in preparation

Richer, H. B. 2001, in proceedings of "The Dark Universe: Matter, Energy and Gravity" (astro-ph/0107079)

Sahu, K. C. 1994, Nature, 370, 275

Smith, C. R., Rest, A., Hiriart, R., Becker, A., Stubbs, C., Valdes, F., & Suntzeff, N. 2002, in SPIE conf.: Astronomical Telescopes and Instrumentations, Hawaii, 22-28 Aug. 2002

Stubbs, C. W. 1999, in ASP Conf. Ser. 165: The Third Stromlo Symposium: The Galactic Halo, 503

Udalski, A., Kubiak, M., & Szymanski, M. 1997, Acta Astronomica, 47, 319

van der Marel, R. P. 2001, AJ, 122, 1827

van der Marel, R. P., & Cioni, M. L. 2001, AJ, 122, 1807

Vivas, A. K., et al. 2001, ApJ, 554, L33

Weinberg, M. D., & Nikolaev, S. 2001, ApJ, 548, 712

Wozniak, P. R. 2000, American Astronomical Society Meeting, 197, 0

Yanny, B., et al. 2000, ApJ, 540, 825

Zaritsky, D., & Lin, D. N. C. 1997, AJ, 114, 2545

Zhao, H. 1998, MNRAS, 294, 139

Zhao, H., & Evans, N. W. 2000, ApJ, 545, L35

Zhao, H., Graff, D. S., & Guhathakurta, P. 2000, ApJ, 532, L37

Zhao, H., Ibata, R. A., Lewis, G. F., & Irwin, M. J. 2003, MNRAS, 339, 701

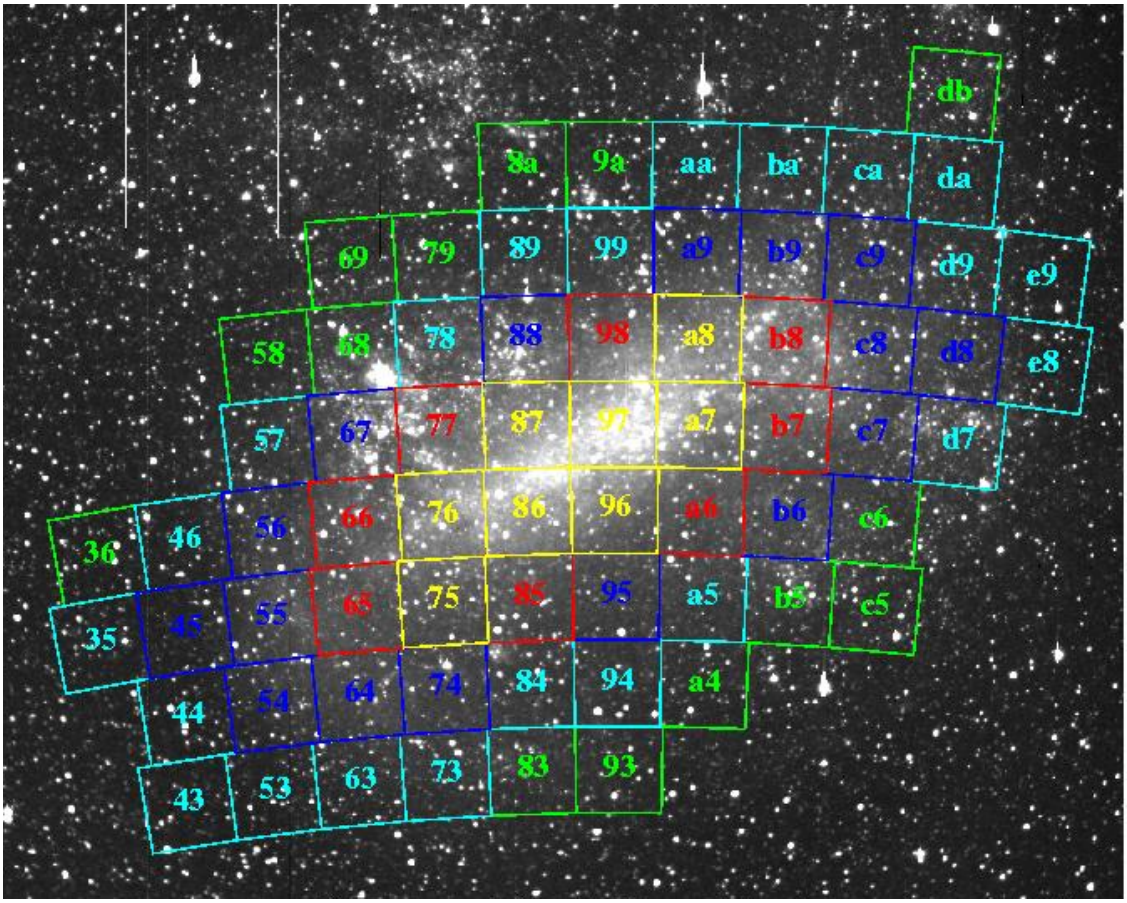

Fig. 1.— SuperMACHO fields superimposed onto the LMC. The fields are divided into sets 1-5, based on their respective star density determined with the Zhao & Evans (2000) LMC bar model. Set 1 is the most crowded (yellow) and set 5 is the least crowded set (green). (LMC image courtesy of G. Bothun.)

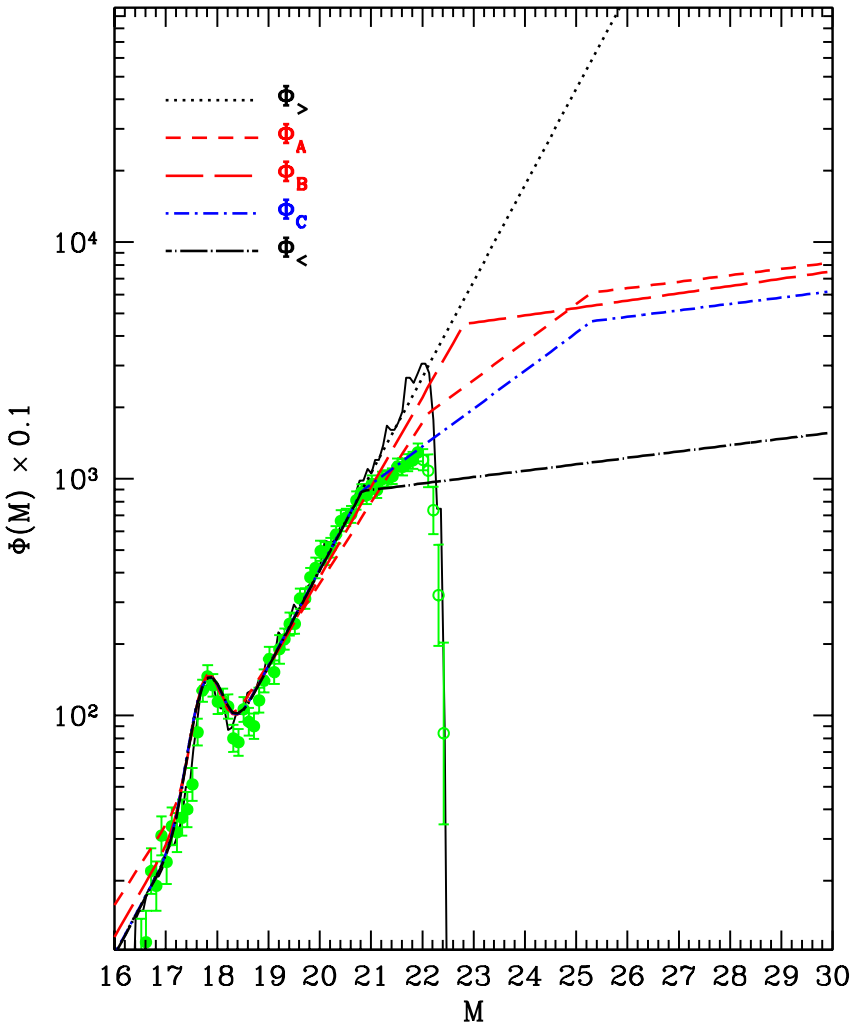

Fig. 2.— Luminosity functions for field sme9. This figure shows the different Luminosity Functions $\Phi_>$, Φ_A, Φ_B, Φ_C, and $\Phi_<$ for the example field sme9. We evaluate the microlensing implications of these different trial luminosity functions. The black dotted line is the bright end LF function parametrized as a single power law ($\Phi_>$) for which the predicted LF (solid line) fits best the observed LF (green filled circles) at the bright end.

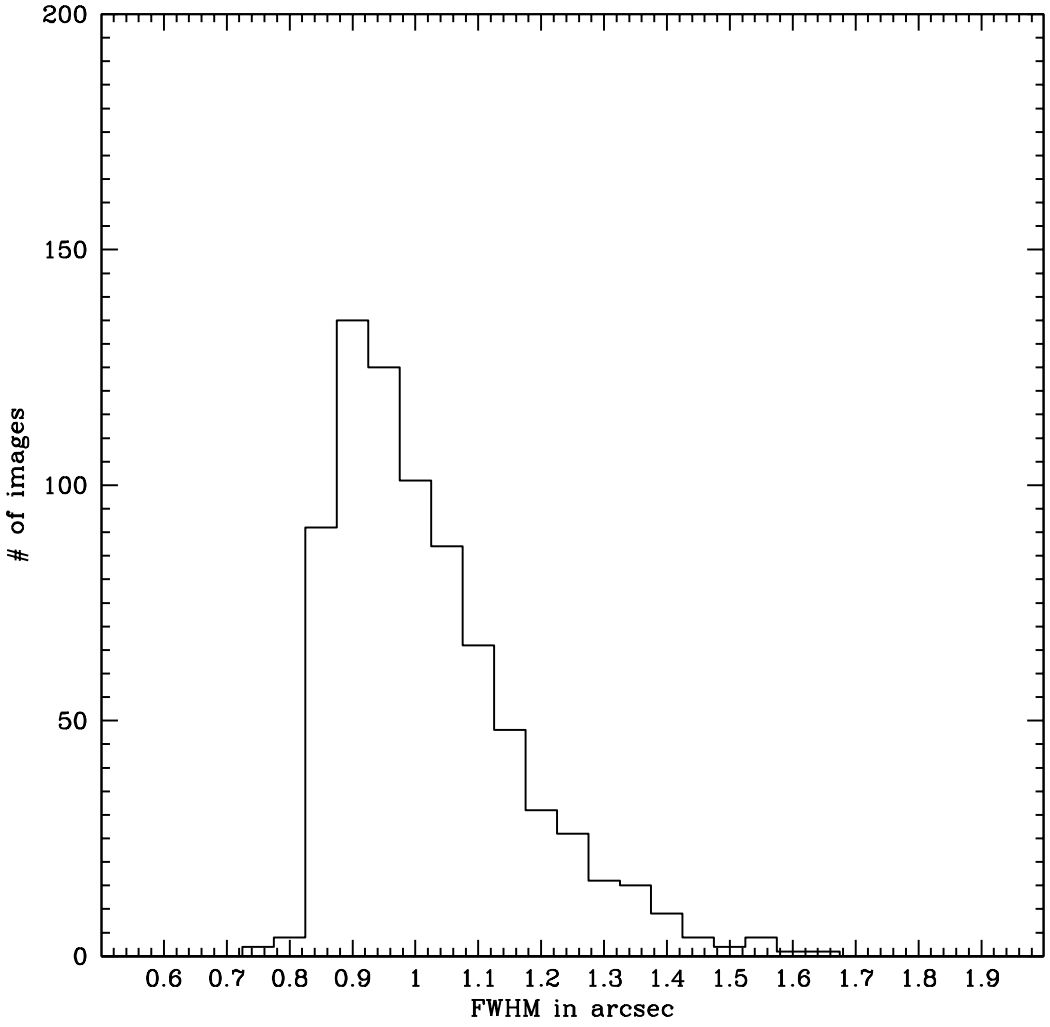

Fig. 3.— Seeing (FWHM) histogram for the 2001/2002 run for amplifier 4. The average is 1.02" with a standard deviation of 0.14.

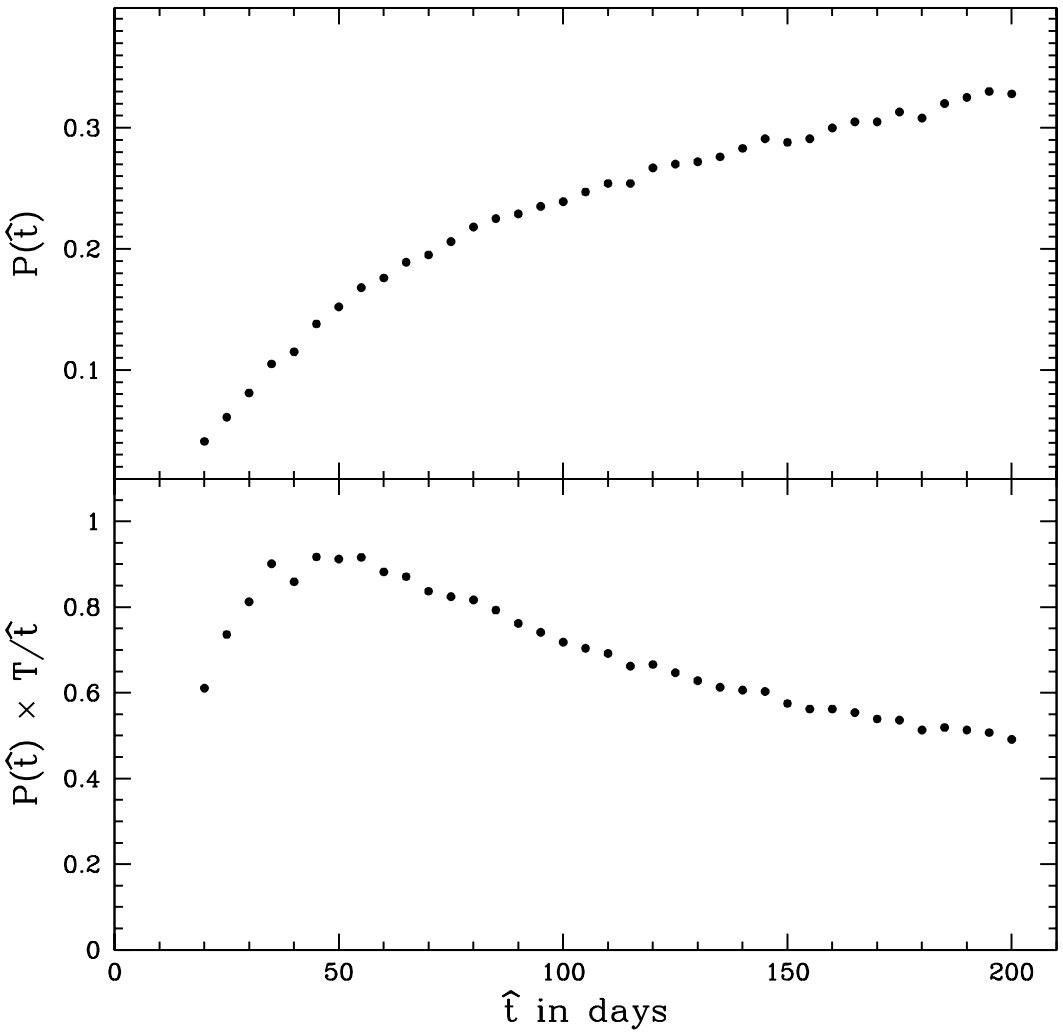

Fig. 4.— Probability of detecting a microlensing event with event duration of $\hat{t}$. The upper panel shows the probability $P\left(\hat{t}\right)$ of detecting a microlensing event with event duration of $\hat{t}$. The lower panel shows the more intuitive measure $P\left(\hat{t}\right) \times T/\hat{t}$, which is the number of microlensing events detected per $1/\tau$ stars during an interval T, assuming that all microlensing events have an event duration of $\hat{t}$. The decrease of detection probability for decreasing event duration is countered by that fact that for shorter event durations more microlensing events happen per $1/\tau$ stars in the given observing time. This causes the peak at $\hat{t} \sim 50$ days.

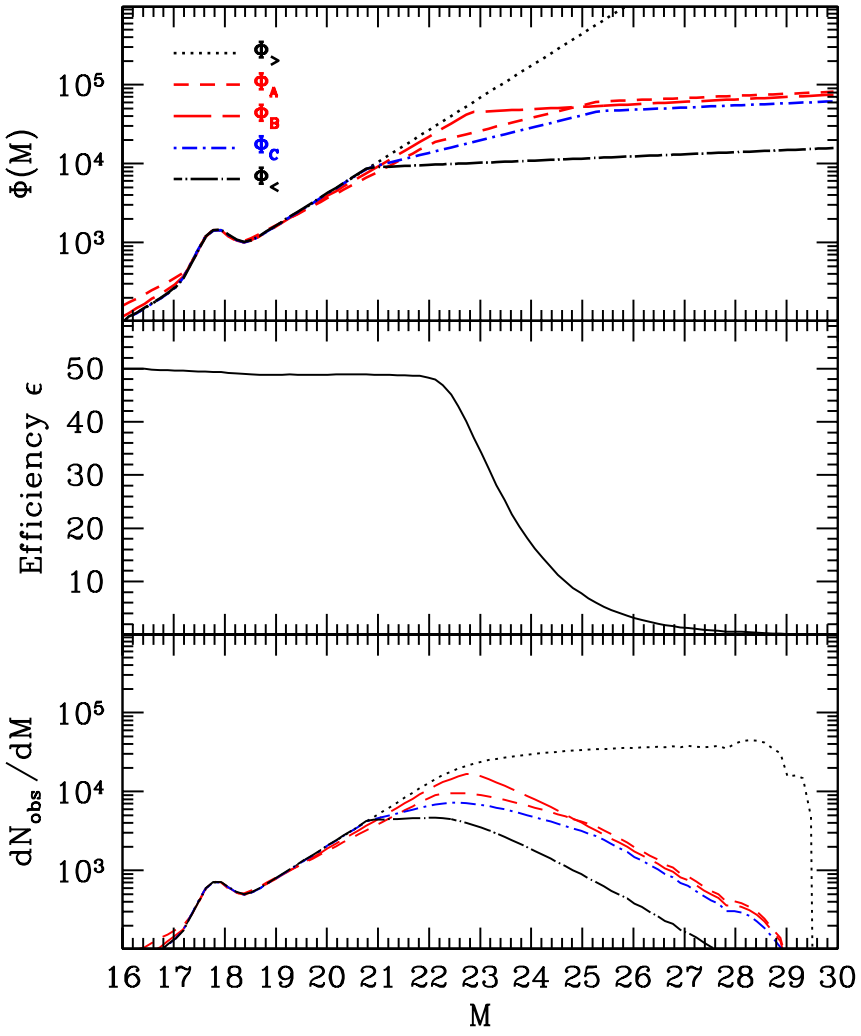

Fig. 5.— Determination of the number of observed stars in field sme9. The upper panel shows the LF candidates $\Phi_>$, Φ_A, Φ_B, Φ_C, and $\Phi_<$, constructed as described in the text. The middle panel shows the event detection efficiency as a function of source star magnitude The lower panel shows the number of useful observed stars vs. magnitude, which is the product of the two upper panels.

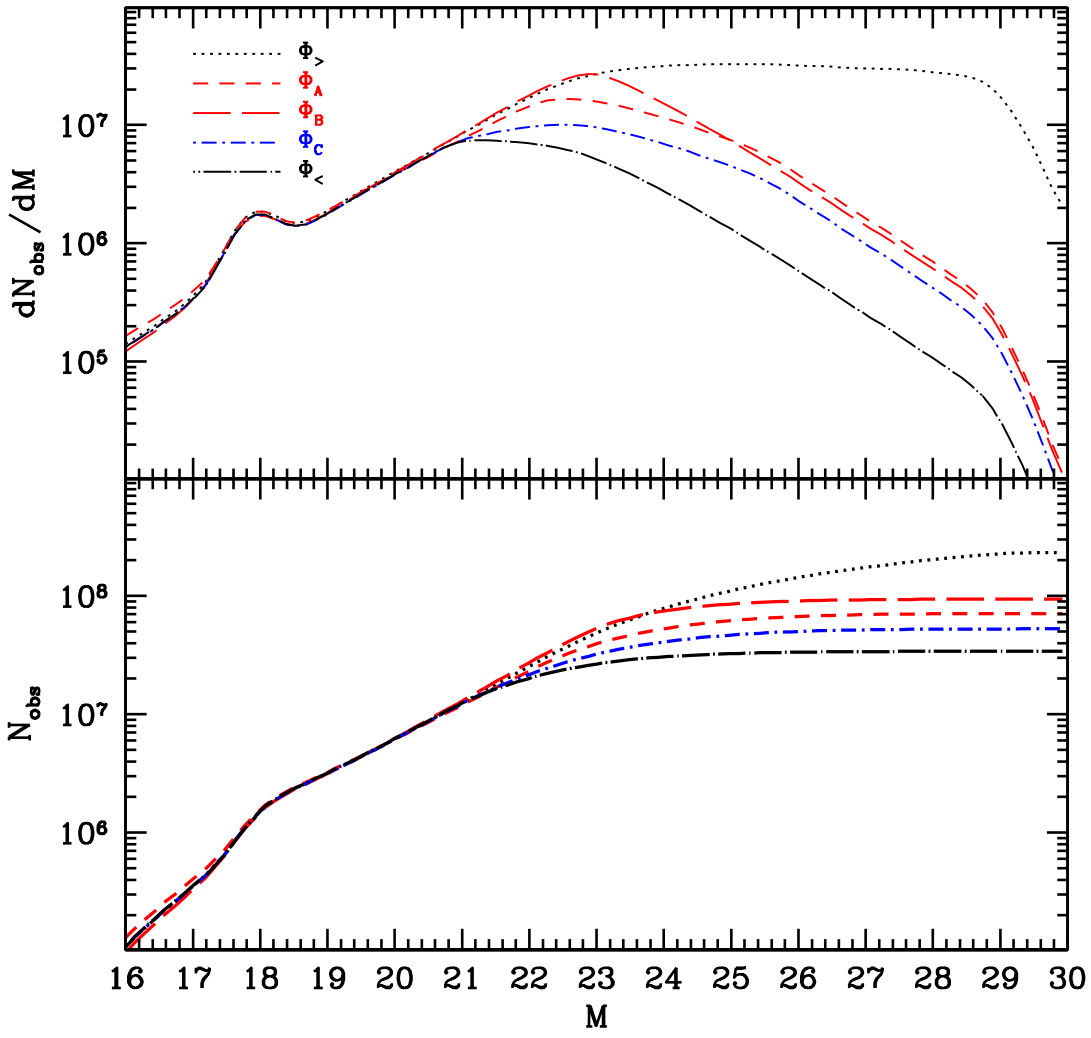

Fig. 6.— Differential and cumulative N_{obs} for different LFs. The upper panel shows the number of observed stars per magnitude bin for all observed fields parameterized by luminosity function. The cumulative number of observed stars is then obtained by integrating over magnitude (see lower panel). The trial LFs $\Phi_>$, Φ_A, Φ_B, Φ_C, and $\Phi_<$, are described in the text.

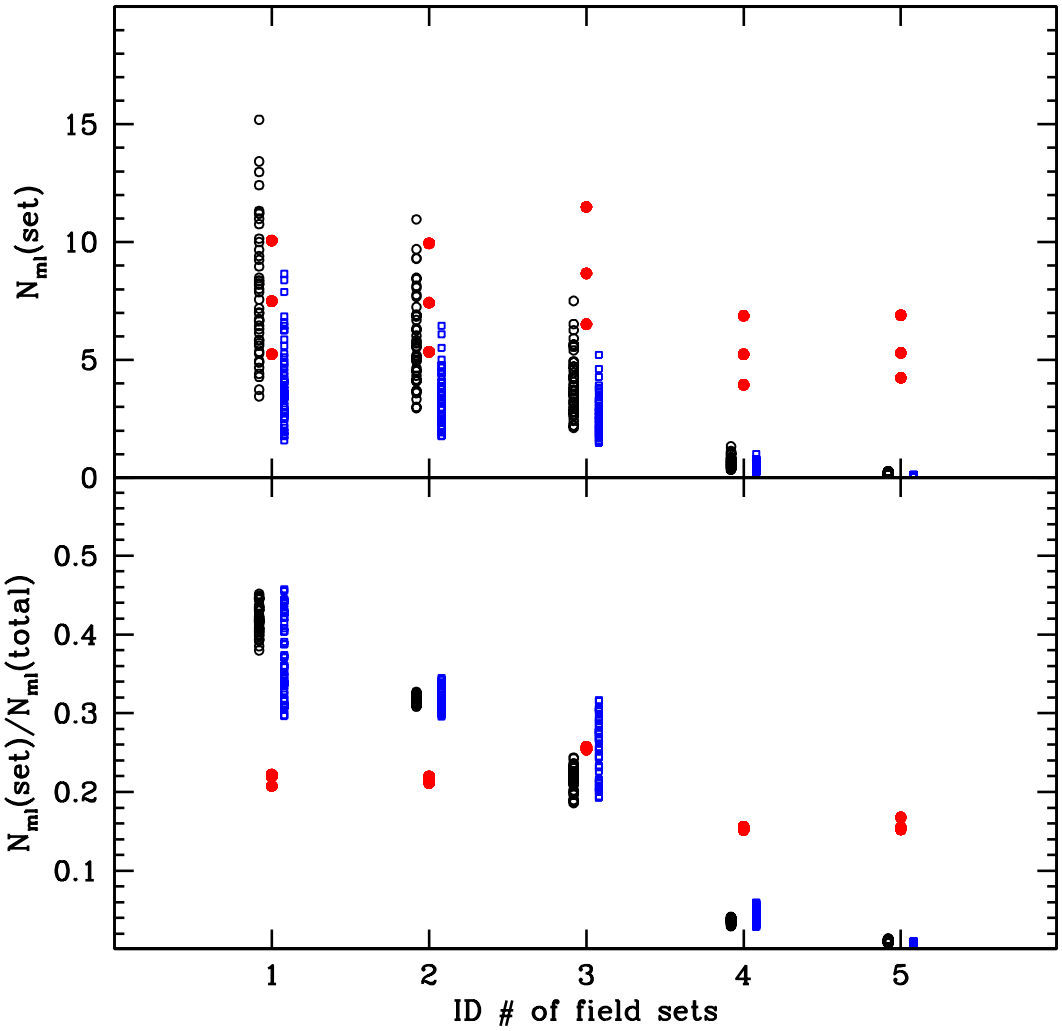

Fig. 7.— Estimated microlensing event rates and differential event rates for the different field sets, as shown in Figure 1. The solid red circles indicate screen-lensing for the different LFs. The Zhao & Evans LMC self-lensing model sets *A* and *B* are indicated with open black circles and blue squares, respectively. The disk-bar displacement of the LMC models varies between -1 and 1 kpc, and the bar mass fraction varies between 0.3 and 0.5. For clarity the open symbols are plotted with a slight offset for a given set. The upper panel shows the event rates as number of events over a 5 year survey. The lower panel shows the differential event rate, normalized to the total number of events detected over the course of the survey. Note that the dependence on the LF's is greatly reduced for the differential rates, as shown in the lower panel. In particular, by comparing the innermost to the outermost fields we expect to be able to distinguish between the screen-lensing and LMC self-lensing scenarios.

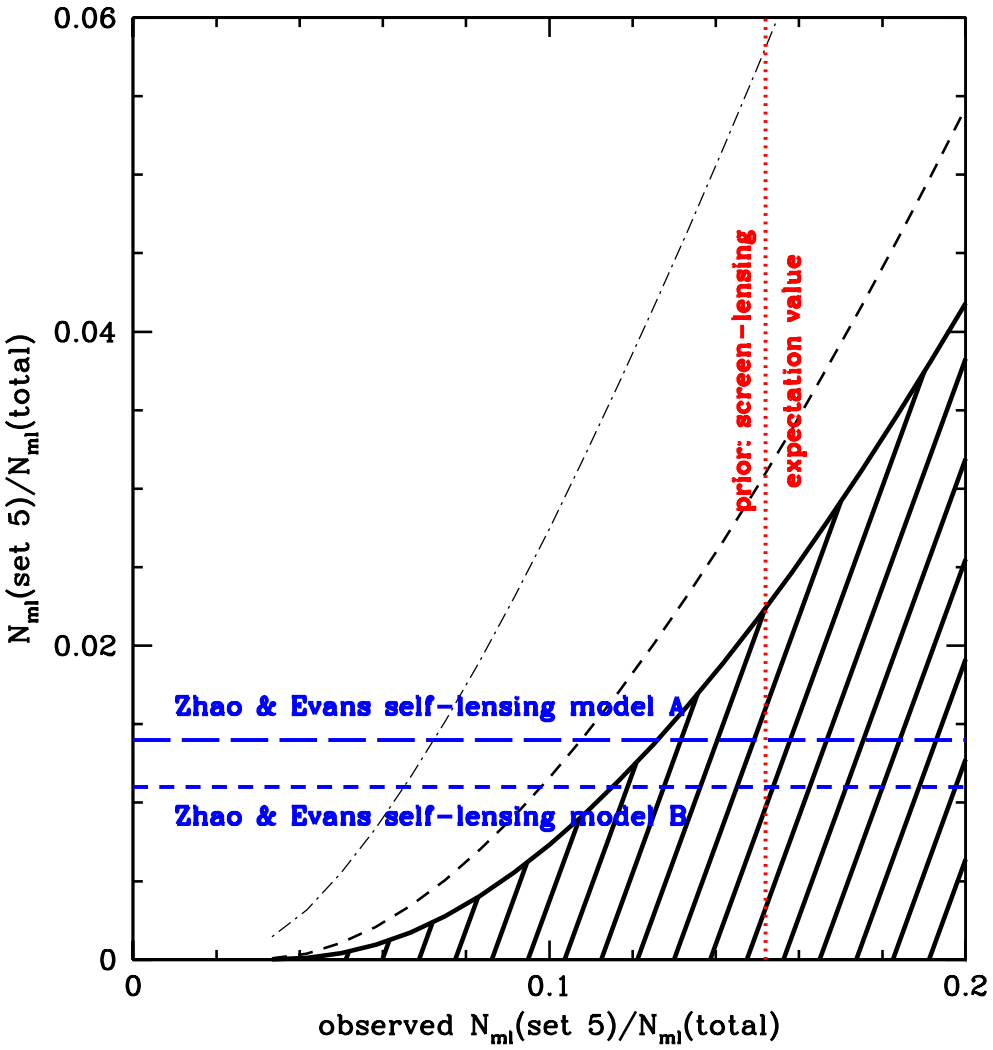

Fig. 8.— Lower limit confidence plots for differential microlensing event rates. The x-axis shows the differential event rate for field set 5 observed by SuperMACHO. The y-axis corresponds to the actual underlying differential rate which SuperMACHO will more tightly constrain. The areas allowed at the 90%, 99%, and 99.5% confidence levels are indicated with dot-dashed, dashed, and solid black lines, respectively, based on Poisson statistics for a total of 30 detected events. So if a differential rate of 0.2 is observed in field set 5, an actual differential rate below 0.04 is excluded at a 99.5% confidence level. The long-dashed and short-dashed horizontal blue lines indicate the *upper* limits for the Zhao & Evans LMC self-lensing model sets A and B, respectively. Thus we would exclude the two LMC self-lensing scenarios with high confidence if over 12% of the detected events occur in field set 5. Table 5 presents the differential rates. The dotted red line indicates the event fraction expected in set 5 for screen-lensing as the dominant mechanism.

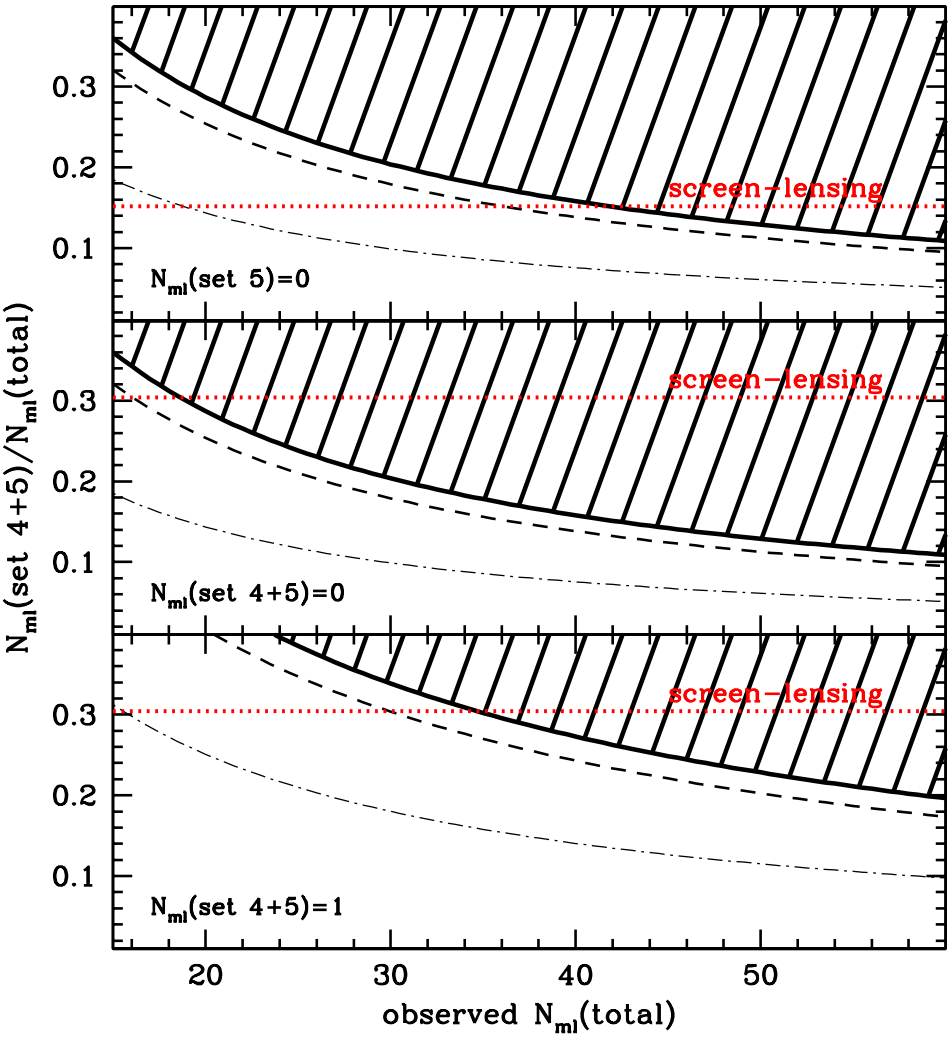

Fig. 9.— Discrimination ability as a function of the number of detected microlensing events. The three panels correspond to different possible experimental outcomes in which few events are detected in the outermost fields. The x-axis shows the total number of detected microlensing events. The y-axis is is the underlying, real differential rate in field sets 4 and 5. The upper panel assumes that no microlensing event is detected in field set 5. The middle and lower panels assuming that zero and one microlensing is detected, respectively, in the outer sets 4 and 5. The 90%, 99%, and 99.5% lower limit confidence levels on the underlying differential rate are indicated with dotted, dashed, and solid black lines. The black shaded areas are thus excluded with at least 99.5% confidence. The dotted red line indicates the *lower* limit for screen-lensing differential rates. For example, in the case where one event is observed in field sets 4 and 5, if a total of 50 microlensing events are detected, an underlying differential rate above 0.23 is excluded at a 99.5% confidence level.

Table 1. SuperMACHO Field Centers and Set Assignment

Field Name	RA (J2000)	Dec (J2000)	Field Set
sm35	06:03:23.10	-70:39:21.1	4
sm36	06:02:13.99	-70:03:20.5	5
sm43	05:58:13.09	-71:51:19.1	4
sm44	05:57:08.79	-71:15:19.8	4
sm45	05:56:08.56	-70:39:18.6	3
sm46	05:55:11.87	-70:03:19.9	4
sm53	05:50:30.80	-71:51:19.0	4
sm54	05:49:40.73	-71:15:18.0	3
sm55	05:48:53.93	-70:39:18.9	3
sm56	05:48:10.11	-70:03:19.4	3
sm57	05:47:28.68	-69:27:16.1	4
sm58	05:46:51.76	-68:51:22.0	5
sm63	05:42:48.49	-71:51:17.1	4
sm64	05:42:13.01	-71:15:18.0	3
sm65	05:41:39.50	-70:39:16.5	2
sm66	05:41:08.07	-70:03:19.1	2
sm67	05:40:38.69	-69:27:18.0	3
sm68	05:40:12.54	-68:51:22.0	5
sm69	05:39:46.29	-68:15:22.0	5
sm73	05:35:06.33	-71:51:40.6	4
sm74	05:34:44.92	-71:15:17.0	3
sm75	05:34:24.88	-70:39:15.9	1
sm76	05:34:06.08	-70:03:18.8	1
sm77	05:33:48.54	-69:27:15.1	2
sm78	05:33:31.74	-68:51:15.6	4
sm79	05:33:16.47	-68:15:37.0	5
sm83	05:27:23.06	-71:51:41.3	5
sm84	05:27:17.12	-71:15:16.5	4
sm85	05:27:10.57	-70:39:17.9	2
sm86	05:27:04.22	-70:03:18.1	1

Table 1—Continued

Field Name	RA (J2000)	Dec (J2000)	Field Set
sm87	05:26:58.38	-69:27:14.8	1
sm88	05:26:52.88	-68:51:15.1	3
sm89	05:26:39.62	-68:15:52.1	4
sm8a	05:26:34.99	-67:39:49.8	5
sm93	05:19:32.39	-71:51:48.3	5
sm94	05:19:39.78	-71:15:52.2	4
sm95	05:19:56.56	-70:39:16.7	3
sm96	05:20:02.60	-70:03:17.5	1
sm97	05:20:08.40	-69:27:16.5	1
sm98	05:20:13.60	-68:51:12.6	2
sm99	05:20:18.91	-68:15:13.4	4
sm9a	05:20:16.08	-67:39:50.7	5
sma4	05:12:11.75	-71:15:53.3	5
sma5	05:12:42.10	-70:39:14.8	4
sma6	05:13:00.96	-70:03:17.4	2
sma7	05:13:18.87	-69:27:12.0	1
sma8	05:13:35.52	-68:51:10.5	1
sma9	05:13:50.38	-68:15:14.4	3
smaa	05:13:57.30	-67:39:50.4	4
smb5	05:05:17.18	-70:39:53.5	5
smb6	05:05:58.98	-70:03:17.9	3
smb7	05:06:28.62	-69:27:17.1	2
smb8	05:06:56.29	-68:51:12.6	2
smb9	05:07:22.50	-68:15:13.0	3
smba	05:07:47.05	-67:39:13.2	4
smc5	04:58:02.60	-70:39:52.3	5
smc6	04:58:46.75	-70:03:54.5	5
smc7	04:59:38.54	-69:27:17.3	3
smc8	05:00:17.34	-68:51:13.8	3
smc9	05:00:53.90	-68:15:13.8	3

Table 1—Continued

Field Name	RA (J2000)	Dec (J2000)	Field Set
smca	05:01:28.43	-67:39:12.9	4
smd7	04:52:48.68	-69:27:18.4	4
smd8	04:53:40.12	-68:51:16.6	3
smd9	04:54:25.76	-68:15:13.4	4
smda	04:55:10.13	-67:39:11.1	4
smdb	04:55:52.16	-67:03:10.6	5
sme8	04:47:00.17	-68:51:17.1	4
sme9	04:47:57.26	-68:15:13.7	4

Note. — SuperMACHO field centers and the field set they are assigned to.

Table 2. Luminosity Function Parameterization

LF	Φ_1	β_1	β_2	β_3	M_1	M_2
(1)	(2)	(3)	(4)	(5)	(6)	(7)
$\Phi_>$	Φ_0	β	-	-	-	-
Φ_A	Φ_{A0}	0.34	0.16	0.027	$M_{RC}+4.3$	$M_{RC}+7.5$
Φ_B	Φ_{B0}	0.38	0.031	-	$M_{RC}+5.0$	-
Φ_C	Φ_0	β	0.16	0.027	$M_{RC}+3.0$	$M_{RC}+7.5$
$\Phi_<$	Φ_0	β	0.027	-	$M_{RC}+3.0$	-

Note. — Overview of the different luminosity function (LF) parameterizations used for computing the number of monitored sources, in the terminology used in the text. Column (1) shows the name of the LF model. Column (2) indicates the normalization factors from that were used. Columns (3)-(5) indicate the relevant power law slopes, if applicable. Columns (6) and (7) show the transition magnitude between power-laws with respect to the fitted red clump magnitude M_{RC}.

Table 3. LMC model parameters

Parameter	Disk	Bar
Inclination i (deg)	25	50
Position Angle θ (deg)	170	120
Δ:W:L (kpc)	0.10:1.35:1.5	0.25:0.67:2
Center	($5^{\rm h}18^{\rm m}$, $-69^\circ.0$, $50.33 - Z_0$ kpc)	($5^{\rm h}24^{\rm m}$, $-69^\circ.8$, 50.00 kpc)
Mass ($M_\odot$)	2.5×10^9	$(1 - 2.5) \times 10^9$

Note. — Parameters used for the LMC disk and bar models.

Table 4. Predicted Microlensing Event Rates for the SuperMACHO Survey

Lens Pop. (1)	Field Set (2)	Min (3)	Mean (4)	Max (5)
screen-lensing	5	4.2	5.5	6.9
	4+5	8.2	10.8	13.8
	all	25.2	34.9	45.2
LMC self-lensing	5	0.12	0.18	0.28
model set *A*	4+5	0.47	0.87	1.6
	all	9.1	18.7	35.3
LMC self-lensing	5	0.03	0.07	0.13
model set *B*	4+5	0.25	0.53	1.13
	all	5.2	10.7	21.4

Note. — Predicted microlensing event totals for a 5 year SuperMACHO survey, for screen and self-lensing scenarios. The lens population and field set are indicated in column (1) and column (2), respectively. The minimum, mean, and maximum event rates for the different models and LFs are shown in column (3), (4), and (5), respectively. The Zhao & Evans LMC self-lensing model set *A* and *B* differ as described in Section 4.3. Note that independent of the overall rate normalization, the *ratios* of rates are a clear and robust indicator of the nature of the lensing population.

Table 5. Predicted Event Rate Ratios

Lens Pop. (1)	Field Set (2)	Min (3)	Mean (4)	Max (5)
screen-lensing	5	**0.15**	0.16	0.17
	4+5	**0.30**	0.31	0.32
LMC self-lensing	5	0.008	0.010	**0.014**
model set *A*	4+5	0.038	0.047	**0.055**
LMC self-lensing	5	0.004	0.007	**0.011**
model set *B*	4+5	0.032	0.051	**0.070**

Note. — Predicted differential microlensing event rates for screen and self-lensing. The lens population and field set is indicated in column (1) and column (2), respectively. The minimum, mean, and maximum differential rates for the different models and LFs are shown in column (3), (4), and (5), respectively. In order to be conservative, we use the minimum values for screen-lensing and the maximum values for self-lensing, indicated in bold. The Zhao & Evans LMC self-lensing model set *A* and *B* differ as described in Section 4.3. Note that independent of the overall rate normalization, the *differential* rates are a clear and robust indicator of the nature of the lensing population.